Engineering Analysis with Boundary Elements 178 (2025) 106322

Contents lists available at ScienceDirect

Engineering Analysis with Boundary Elements

journal homepage: www.elsevier.com/locate/enganabound

A fast directional boundary element method for solving wideband three-dimensional half-space acoustic problems

Haoyang Li, Yijun Liu *

Department of Mechanics and Aerospace Engineering, Southern University of Science and Technology, Shenzhen, 518055, PR China

ARTICLE INFO

Keywords:
Fast directional algorithm
Fast multipole method
Boundary element method
Half-space problems
Acoustic wave problems

ABSTRACT

This paper presents a novel wideband fast multipole boundary element method (BEM) based on a fast directional algorithm (FDA) for solving large-scale three-dimensional (3-D) half-space acoustic wave problems. The method employs the half-space Green's function in the boundary integral equations, eliminating the need to discretize the infinite plane and avoiding truncation errors. An improved FDA is developed to expand the kernel functions, enabling efficient matrix-vector product acceleration across a wide range of frequencies. Unlike full-space problems, the translations for half-space problems differ due to the half-space Green's function. Leveraging the symmetry of the half-space problem, we introduce techniques to reduce the computational cost in fast multipole translations. Specifically, only an additional moment-to-local (M2L) translation for the image part is required, bypassing the computation and storage of other image-related translations. The iterative solver GMRES is used to further accelerate the solution in the proposed FDA-BEM. Numerical examples validate the accuracy of the method and demonstrate its nearly linear computational efficiency in solving large-scale 3-D half-space acoustic problems. Large scale models with the nondimensional wavenumber above 400 and number of elements above 3 million have been solved successfully using the developed method.

1. Introduction

The boundary element method (BEM) has been widely applied to solve exterior acoustic problems [1–10], because only the boundary discretization is required and the Sommerfeld radiation condition at infinity is naturally satisfied. For full-space problems, the Green's function G is utilized to formulate the boundary integral equation (BIE). When considering half-space problems, the BIE can also be obtained by using G, however it will lead to the need for discretizing the infinite half-space plane. Using an alternative approach, a new kernel function can be derived for half-space problems to eliminate the integral on the infinite plane [11–15]. For half-space problems, the source solution at the image point is to be added to full-space Green's function whether the infinite plane is rigid (zero velocity) or soft (zero sound pressure). By applying the half-space Green's function, the advantage of boundary-only discretization of the structure is maintained and the truncation error in discretizing the infinite plane is avoided.

There are several types of fast algorithms to accelerate the matrix-vector product in the acoustic BEM when dealing with large scale acoustic problems, such as the fast multipole method (FMM) [16]. Based on analytical series expansions of the kernel functions, the original FMM was proposed by Greengard and Rokhlin to solve N-body problems governed by Laplace equation. For low-frequency acoustic problems, the Green's function of Helmholtz equation shares similar properties as for the Laplace equation. A similar analytical expansion based on spherical harmonics has been widely used in the low-frequency FMM [4,14, 17–19]. As the frequency increases, such expansion applied on low-frequency domain does not perform well on high-frequency domain due to the larger number of expansion terms. The analytical diagonal form FMM and various improved methods have been widely studied in order to improve the performance of the FMM at higher frequencies (see, e.g., Refs. [20–22]). It is noted that the diagonal form FMM is not suitable for low-frequency problems due to the numerical instability. Combining the advantages of the above two methods, the hybrid wideband FMM utilizing two types of expansions have been developed for full-space problems [23–27].

However, all the above mentioned FMMs based on the analytical expansions of the kernels are kernel dependent. For some Green's functions, it is difficult to obtain the efficient analytical expansion expressions. The kernel independent FMM (KIFMM) proposed by Ying

* Corresponding author.
E-mail address: liuyj3@sustech.edu.cn (Y. Liu).

https://doi.org/10.1016/j.enganabound.2025.106322
Received 10 February 2025; Received in revised form 23 May 2025; Accepted 23 May 2025

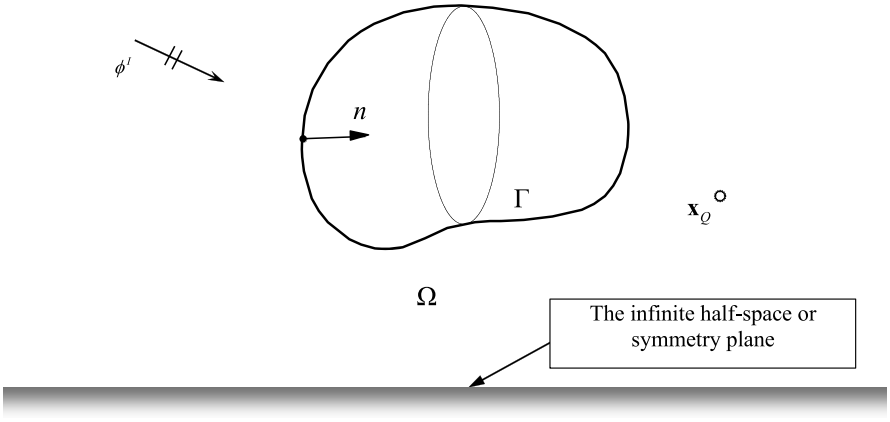

Fig. 1. A half-space acoustic wave problem.

et al. [28] requires no analytical expansions, which makes FMM more versatile when dealing with different type of problems. Different from the analytical expansion based FMM, a set of equivalent density and potential checking points is established and the multipole expansion construction is replaced by solving local exterior inverse problems in KIFMM. Although a rigorous error analysis is difficult to obtain for KIFMM, many numerical examples reported in the literature have confirmed its accuracy and stability [29,30]. As the frequency increases, too many expansion items in the KIFMM still limit its efficiency in solving large-scale problems. However, the directional low rank property of the oscillatory kernels has been confirmed and utilized successfully in various fast directional algorithms [31–37]. Based on the directional low rank property of the oscillatory kernels, the FMM with fast directional algorithm (FDA), which is a high-frequency version of KIFMM, is able to accelerate summations when the kernel is of high oscillation [32,36].

In this paper, we present a novel wideband fast multipole BEM based on the FDA for solving large-scale 3-D half-space acoustic wave problems. The fast multipole method based on FDA is developed not only because of its versatility, but also because of its performance at high frequencies. In three-dimensional problems, the analytical diagonal form FMM still faces the problem of too many analytical expansion items at extremely high frequencies, i.e. the dimensionless wavenumber is above 400 or 500. In contrast, the number of expansion terms in FDA does not change with the wavenumber under certain conditions, which enables the FDA-based FMM to achieve high computational efficiency at high frequencies. Methods based on similar ideas, for example, the proxy surface (or point) methods [38–40] and recursive skeletonization approaches have been utilized in the development of fast direct solvers [41–46].

It is noted that the matrix low-rank decomposition of the original FDA-based FMM is computationally cumbersome and may lead to numerical instability, therefore, reducing the computational accuracy. In this paper, an improved method is proposed to construct the matrix decomposition. By using potential theory and introducing posteriori estimates, the sample point space is greatly compressed, resulting in a very small sample matrix to be operated. Then the overall computational complexity of subsequent matrix decomposition is relatively low, and the matrix decomposition using direct deterministic algorithm is more stable.

Additionally, we extended the FDA-based FMM from full-space to half-space firstly. Based on the symmetry of the half-space problem, a few techniques are developed to reduce the computation of the fast multipole translations. Only additional moment to local (M2L) translation for the new image part is needed, thus avoiding the computation and storage of other translations for the image part in the kernels. Some simplification techniques are used to further decrease the additional computation of M2L translations.

The paper is organized as follows: In Section 2, the basic BIEs for half-space acoustic problems are reviewed. In Section 3, the kernel expansions and an optimized point-sampling scheme in using FDA are described. In Section 4, the algorithms for half-space problems are described in detail. In Section 5, numerical examples are presented to demonstrate the accuracy and efficiency of the developed approach. Some conclusions are provided in Section 6.

2. Boundary integral equations for half-space acoustic problems

The governing differential equation of the acoustic problem in the frequency domain can be written as the well-known Helmholtz equation:

$$\nabla^2\phi(\mathbf{x},\omega)+k^2\phi(\mathbf{x},\omega)+Q\delta(\mathbf{x},\mathbf{x}_Q)=0 \tag{1}$$

in which $\phi(\mathbf{x},\omega)$ is the sound pressure, Q the intensity of a point source, k the wavenumber. As shown in Fig. 1, two types of boundary conditions are considered:

$$\begin{cases}\phi=\widehat{\phi},\mathbf{x}\in\Gamma_{\mathrm{D}}\\ q\equiv\dfrac{\partial\phi}{\partial n}=\widehat{q},\mathbf{x}\in\Gamma_{\mathrm{N}}\end{cases} \tag{2}$$

where the over hat symbol denotes the given quantity on the boundary, n is the unit outward normal direction, q denotes the normal derivative of ϕ, and $\Gamma=\partial\Omega=\Gamma_{\mathrm{D}}+\Gamma_{\mathrm{N}}$ represents the boundary of the computation domain Ω.

Applying the second Green's identity and utilizing the properties of Dirac-δ function, the following conventional boundary integral equation (CBIE) can be obtained for a field point $\boldsymbol{x}$ inside the domain Ω [10]:

$$\phi(\mathbf{x})=\int_\Gamma[G(\mathbf{x},\mathbf{y})q(\mathbf{y})-F(\mathbf{x},\mathbf{y})\phi(\mathbf{y})]\mathrm{d}\Gamma(\mathbf{y})+\phi^I(\mathbf{x})+QG(\mathbf{x},\mathbf{x}_Q) \tag{3}$$

in which ϕ^I denotes the incident wave for scattering problems, G is the Green's function (fundamental solution) for full-space problems given as:

$$\begin{cases}G(\mathbf{x},\mathbf{y})=\dfrac{1}{4\pi r}e^{\mathrm{i}kr}\\ F(\mathbf{x},\mathbf{y})\equiv\dfrac{\partial G(\mathbf{x},\mathbf{y})}{\partial n(\mathbf{y})}\end{cases} \tag{4}$$

where $r=|\mathbf{x}-\mathbf{y}|$ is the distance between the field point $\boldsymbol{x}$ and source point $\boldsymbol{y}$.

For an exterior half-space problem, CBIE (3) with expression (4) can also be used with increased computational cost, because not only the

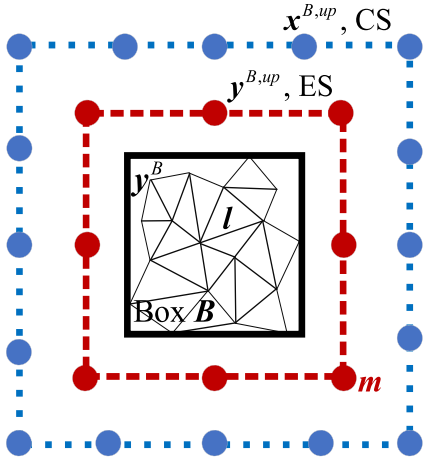

Fig. 2. Equivalent source approximation in the KIFMM. Given sources inside the box B, for example triangular boundary elements, the equivalent sources (the red dots) on the equivalent surface ES (the red dotted line) can be obtained by two steps: firstly, evaluating the equivalent sources (the blue dot) on the check surface CS (the blue dotted line), and secondly solving a Dirichlet problem inversely.

boundary of the structure, but also the infinite plane has to be a part of boundary of the computation domain. As a result, the infinite plane is often artificially cut off to form a finite area for the convenience of implementation, resulting in loss of the computational accuracy.

In a more efficient approach, the Green function G^* for half-space problems [12] can be derived and utilized to obtain the BIE similar to Eq. (3). In this way, only the boundary of the structure needs to be discretized, avoiding the computation on the infinite plane. The new BIE and fundamental solutions can be expressed as [10]:

$$\phi(\mathbf{x}) = \int_\Gamma [G^*(\mathbf{x},\mathbf{y})q(\mathbf{y}) - F^*(\mathbf{x},\mathbf{y})\phi(\mathbf{y})]\mathrm{d}\Gamma(\mathbf{y}) + \phi^*(\mathbf{x}) + QG^*(\mathbf{x},\mathbf{x}_Q) \tag{5}$$

$$\begin{cases} G^*(\mathbf{x},\mathbf{y}) = G(\mathbf{x},\mathbf{y}) + \alpha G(\bar{\mathbf{x}},\mathbf{y}) \\ F^*(\mathbf{x},\mathbf{y}) \equiv \dfrac{\partial G^*(\mathbf{x},\mathbf{y})}{\partial n(\mathbf{y})} \\ \phi^*(\mathbf{x}) = \phi^I(\mathbf{x}) + \alpha\overline{\phi}^I(\mathbf{x}) \end{cases} \tag{6}$$

where $\bar{\mathbf{x}}$ is the mirror image point of the source point $\boldsymbol{x}$ with respect to the infinite plane in the lower half space. The direction of the incident wave $\overline{\phi}^I$ and the direction of the incident wave ϕ^I are symmetrical about the infinite plane. Constant α is the reflection coefficient distinguishing different types of the infinite planes. For a rigid infinite symmetry plane on which the acoustic particle velocity is zero, α is set to be 1; and for a totally soft one on which the pressure is zero, α is set to be -1.

In order to eliminate the error introduced by the fictitious eigenfrequency, the Burton–Miller formulation [47] is applied in this paper. With the combination of the CBIE and its normal derivative, unique solutions for exterior acoustic problems can be obtained [4,35].

In this work, constant triangular surface elements with piecewise linear geometry are used to discretize the boundary. By using constant elements, the case of collocating the BIE at corner nodes do not exit, thus discontinuities of physical quantities at corner nodes between elements need not to be considered. There is also no need to evaluate the free term at each node, which facilitates the computation. With $\partial r/\partial n = 0$ on the singular element for the linear geometry, there are only one singular integral for which the kernel function is G^* in Eq. (5). In this work, an unified method is applied to evaluate singular integrals [2]: according to series expansion, function f' of the same order as the original kernel function f can be obtained; for the first part which integral kernel is $f - f'$, direct Gaussian numerical integration method is applied to evaluate this integral with non-singularity; for the second part which integral kernel is f', the analytical solution can be obtained directly due to its simple expression.

Substituting boundary conditions into the discretized equation based on BIE (5), then moving unknown terms to left-hand side and known terms to right-hand side, a linear system of equations is formed as follows:

$$\mathbf{A}\lambda = \mathbf{b} \tag{7}$$

where $\boldsymbol{A}$ is the system matrix, λ is a vector containing unknown pressure or velocity on the boundary, and $\boldsymbol{b}$ is the known vector corresponding to sources and known values on boundary. In general, without specific translations, matrix $\boldsymbol{A}$ is full and asymmetric, resulting in $O(N^2)$ memory storage and $O(N^3)$ computation complexity using conventional direct solvers. The computational cost greatly limits the application of the BEM in solving large scale engineering problems. To overcome this shortcoming, some efforts have been devoted to improving the computational efficiency of the BEM, such as the fast multipole method. Applying FMM with an iterative solver (for example the GMRES), the computational cost can be reduced to an approximately optimal complexity of $O(N)$, as well as for the memory storage.

3. Translations and formulations of wide-band FDAFMM

For the FDA or KIFMM, both the kernel function itself as the interpolation basis or use the rows and columns of the matrix itself to perform low-rank approximation can be applied. Unlike the analytical expansion-based FMM, which requires different series expansions for different kernels, KIFMM or FDA can use the same expansion for different kernels. At the same time, this expansion form has a clear physical meaning, which is also one of its advantages. In the following, the expansions of the kernel functions at different frequencies and the fast algorithm for solving the half-space problem will be presented.

3.1. Basic translations in KIFMM on low-frequency domain

According to the potential theory, for any kernel derived from second-order linear elliptic partial differential equations, the same potential distribution in a specified domain can be obtained by using different source distributions. Furthermore, if the potential distribution on the boundary is determined, then the potential at each particle in the domain will also be determined uniquely.

More specifically, for some source items $\boldsymbol{q}^B$ distributed within the box B, whether discrete or continuous, a different source distribution $\boldsymbol{q}^{B,up}$ located on the equivalent surface (ES) $\boldsymbol{y}^{B,up}$ is applied to approximate them as equivalent sources, so that the two sets of source distributions produce approximately the same potential in the far field $\boldsymbol{x}^{B,far}$. In order to obtain the equivalent source distribution, a check surface (CS) $\boldsymbol{x}^{B,up}$ is set up so that the potential field $\boldsymbol{\phi}^{B,up}$ generated by the two sets of source distributions on this surface are consistent.

$$\phi_n^{B,up} = \sum_l G\left(x_n^{B,up}, y_l^B\right) q_l^B = \sum_m G\left(x_n^{B,up}, y_m^{B,up}\right) q_m^{B,up} \tag{8}$$

Eq. (8) can be expressed in a matrix form:

$$\boldsymbol{E}^B\boldsymbol{q}^B = \boldsymbol{E}^{B,up}\boldsymbol{q}^{B,up} \tag{9}$$

In practice, the number of check points is larger than the number of equivalent points. Denotes its pseudo inverse matrix as $\left(\boldsymbol{E}^{B,up}\right)^\dagger$, then the equivalent sources $\boldsymbol{q}^{B,up}$ can be obtained:

$$\boldsymbol{q}^{B,up} = \left(\boldsymbol{E}^{B,up}\right)^\dagger \boldsymbol{E}^B\boldsymbol{q}^B = \boldsymbol{M}^B\boldsymbol{q}^B \tag{10}$$

The above equation is regarded as the multipole to multipole (M2M) translation in KIFMM, and $\boldsymbol{M}^B = \left(\boldsymbol{E}^{B,up}\right)^\dagger \boldsymbol{E}^B$ is the M2M translation

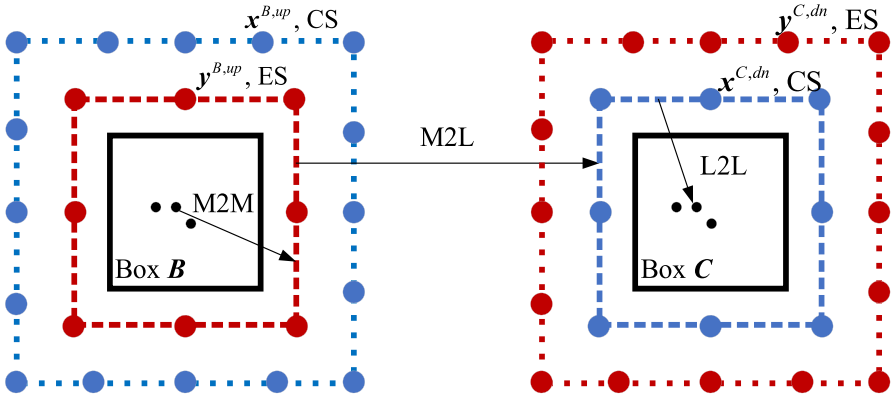

Fig. 3. M2M, M2L and L2L translations in the KIFMM.

matrix. On the upward pass, $\boldsymbol{x}^{B,up}$ and $\boldsymbol{\phi}^{B,up}$ are also called the upward CS and upward check potential; $\boldsymbol{y}^{B,up}$ and $\boldsymbol{q}^{B,up}$ are called the upward ES and equivalent sources.

Some comments on Eqs. (8)-(10) are given as following:

(1) In order to guarantee the smoothness of the potential in far field $\boldsymbol{x}^{B,far}$ produced by the equivalent source $\boldsymbol{q}^{B,up}$, there should be no intersection between $\boldsymbol{x}^{B,far}$ and CS $\boldsymbol{y}^{B,up}$ (or box B). And $\boldsymbol{y}^{B,up}$ needs to enclose box B to make sure the potential produced by $\boldsymbol{q}^{B,up}$ and $\boldsymbol{q}^{B}$ in the far field is consistent. Combining the above two conditions, the upward ES and CS in the upward pass are set as shown in Fig. 2: $\boldsymbol{y}^{B,up}$ is sandwiched between box B and $\boldsymbol{x}^{B,up}$. Furthermore, by changing the distance between the ES and the CS, the calculation accuracy of the equivalent source approximation can be adjusted. Considering the analytical FMM, the truncation error can be expressed as $\frac{1}{l+1}\left(\frac{R_1}{R_2}\right)^{l+1}\frac{R_1}{R_2-R_1}$, where l represents the number of truncation terms in the analytical expansion, the maximum value of R_1 is the distance between the box center and the point farthest from the center in the grid, and the minimum value of R_2 is the distance between the box center and the source term conversion area [16,23]. A smaller truncation error requires a larger number of truncation terms l and a smaller ratio R_1/R_2. Similar to the analytical FMM, increasing the distance between the ES and the CS and increasing the number of equivalent sources can reduce the error of the equivalent source approximation in KIFMM.

(2) The source field distribution is represented by the point source intensity in Eq. (8), which is in discrete form. For an alternative way, the potential field can be calculated by integrating the source density on the equivalent surface. In practice, this method of calculating the potential field in the form of an integral is not used in M2M. Because it is difficult to find an appropriate quadrature rule to calculate the integral on an arbitrary surface with both high precision and computational efficiency. In numerical computation, it was found that the required accuracy can be obtained with a small number of point sources distributed on the boundary of a sphere or a cube, which is consistent with the conclusion in previous references [28,30].

(3) The single-layer potential, kernel G is used to represent the potential produced by the equivalent source on the right hand side in Eq. (8), where each discrete equivalent source can be regarded as a monopole. When the left side of Eq. (8) is the potential generated by double-layer potential F, for example the boundary integrals containing kernel F, it is natural to use F to calculate the potential on the right hand side of Eq. (8). Indeed, kernel G can also be applied to compute the potential generated by kernel F. Considering the physical meaning, G represents a monopole at $\boldsymbol{y}$ which produces potential at $\boldsymbol{x}$, while F represents a dipole. This approach is actually using a set of monopole sources to equivalently approximate another set of dipole sources, where a dipole consists of two monopoles with opposite phase. Such equivalent source approximation by a unified form with kernel G provides both the computation and storage of the translation matrix.

For a source to multipole (S2M) translation, it is similar to that of M2M, except that the check potential on the left side of Eq. (8) is calculated by the boundary integrals within box B.

Compared to M2M, multipole to local (M2L) translation is relatively easier to understand and implement. According to a summation, the potential on the other box C can be directly evaluated by the known position and intensity of equivalent sources which belongs to box B:

$$f^{C,dn} = \boldsymbol{E}^{B2C}\boldsymbol{q}^{B,up} \tag{11}$$

On the downward pass, in order to further reduce the amount of computation, the spatial location is swapped of ES and CS. Specifically, for a box B, its downward ES share the same surface with the upward CS, and its downward CS share the same surface with the upward ES. Then, local to local (L2L) translation can be regarded as a reverse process of M2M:

$$f^{B} = \boldsymbol{L}^{B}f^{B,dn} \tag{12}$$

The L2L translation matrix can be obtained directly by transposing M2M translation matrix on the upward pass, $\boldsymbol{L}^{B} = \left(\boldsymbol{M}^{B}\right)^{T}$.

So far, all translations have been briefly described, and a single layer for KIFMM translations is shown in Fig. 3.

According to the M2M translation, we obtain the upward equivalent sources (the red dots on the left) which can approximate the potential field produced by sources (the dark dots on the left) inside the box B. Then we use the upward equivalent sources on the red equivalent surface of box B to evaluate the downward check potentials (the blue dots on the right) on the bule check surface of box C. According to the L2L translation, we get the downward check potentials (the dark dots on the right) inside the box B from the downward check potentials on the blue check surface of box C.

3.2. Basic translations in FDAFMM on high-frequency domain

With the increase of the dimensionless wavenumber ka, where a denotes a characteristic length, a few problems arise if we continue to apply the expansion format used in KIFMM. The oscillation characteristic of the kernel function becomes more and more significant as the wavenumber k increases. Similar to other types of expansion applied on low-frequency domain, when it is applied directly on high-frequency

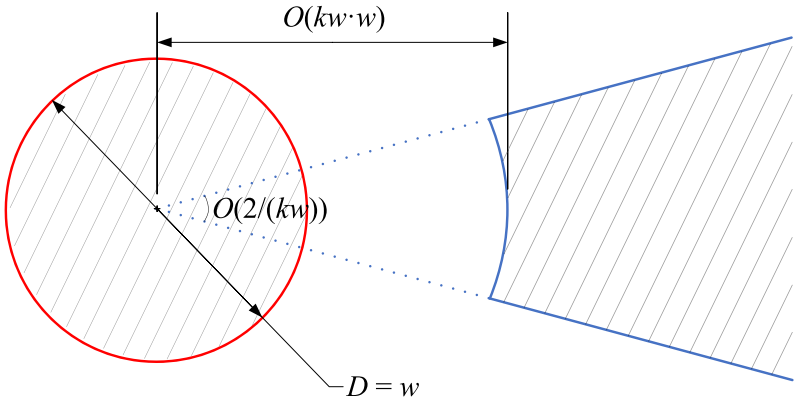

Fig. 4. The directional parabolic separation condition.

domain, a large number of interpolation bases are needed to meet the required accuracy, and the number grows approximately linearly with k. In KIFMM, it means that more equivalent points are required, and the larger transforming matrix results in more computing time. This cumbersome amount of computation goes against the original intention of fast algorithms. On the other hand, using the expansion form of the low-frequency algorithm will also bring certain computational stability issues.

Some efforts have been devoted to studying characteristics of high-frequency oscillating kernel functions. In reference [32,36], researchers have proved that the oscillating kernel function can be expanded with bounded truncation terms in a given direction, provided that it satisfies the directional parabolic separation condition. The two clusters X and Y that satisfy this geometric configuration can be defined as follows:

$$\begin{cases} Y = \{\boldsymbol{y} : |\boldsymbol{y} - \boldsymbol{c}_Y| \le w/2\} \\ X = \{\boldsymbol{x} : |\boldsymbol{x} - \boldsymbol{y}| \ge O(kw^2), \quad \theta(\boldsymbol{x} - \boldsymbol{y}, \boldsymbol{l}) \le O(1/kw)\} \end{cases} \tag{13}$$

As shown in Fig. 4, w denotes the diameter of a circle (or sphere in 3D) Y and $\boldsymbol{c}_Y$ is the center of Y, $\theta(\cdot,\cdot)$ represents the angle between the two directions and $\boldsymbol{l}$ is a given direction. Then, for any $\boldsymbol{x} \in X$ and $\boldsymbol{y} \in Y$, the following directional separated representation is valid:

$$\left| G(\boldsymbol{x},\boldsymbol{y}) - \sum_{i=1}^{T(\varepsilon)} r_i(\boldsymbol{x}) s_i(\boldsymbol{y}) \right| = O(\varepsilon) \tag{14}$$

in which ε is the tolerance for required accuracy, $T(\varepsilon)$ is the number of expansions, and $r_i(\boldsymbol{x})$ and $s_i(\boldsymbol{y})$ are functions of $\boldsymbol{x}$ and $\boldsymbol{y}$ respectively. It is noted that T only depends on ε and has nothing to do with the underlying wavenumber k in kernel G. According to this property, the expansion of kernel function with different wavenumbers can be unified, which facilitates the construction of the kernel function expansion for wide band problems. In numerical computation, it is found that the number of T is relatively small, which makes it possible to implement fast algorithms in practice.

Since under the guarantee of the directional parabolic separation condition, the kernel G can be expanded with a low order T in a unified format, then the next step is to find suitable basis functions to construct this expansion. For high-frequency domain, the advantage with clear physical meaning in KIFMM is also expected to be maintained. The analogous expansion can be expressed as follows:

$$\left| G(\mathbf{x},\mathbf{y}) - \sum_n G(\mathbf{x},\mathbf{b}_n) \sum_m d_{nm} G(\mathbf{a}_m,\mathbf{y}) \right| = O(\varepsilon) \tag{15}$$

and in matrix form:

$$|\mathbf{G} - \mathbf{G}_c \mathbf{D} \mathbf{G}_r| = O(\varepsilon) \tag{16}$$

where $\{\mathbf{a}_i\}$ and $\{\mathbf{b}_i\}$ are a small set of points which belong to X and Y, respectively, and $\mathbf{D}[d_{nm}]$ is an intermediate transformation matrix. From a matrix perspective, the matrix $\boldsymbol{G}$ can be reconstructed by using part of its own rows and columns with certain accuracy. Different from the analytical expansion for low-frequency FMM, there is no rigorous mathematical theory to accurately estimate the error of its expansion, only a rough estimate of upper limit is available. However, it is believed that the selected rows would serve well as a set of bases to span the entire row vector space of the matrix, and so would the selected columns. Because the rows and columns of the matrix $\boldsymbol{G}$ formed by the kernel itself contain enough oscillation characteristics, which is similar to use functions such as sin and cos to construct its basis.

In FDA, equivalent source and equivalent potential could still be used, with only an additional constraint on the definition. Eq. (15) could be rewritten in another expression with obvious physical meaning as:

$$\left| \sum_i G(\mathbf{x},\mathbf{y}_i) q_i - \sum_n G(\mathbf{x},\mathbf{b}_n) \left(\sum_m d_{nm} \sum_i G(\mathbf{a}_m,\mathbf{y}_i) q_i \right) \right| = O(\varepsilon) \tag{17}$$

Eq. (17) describes such a procedure on the upward pass: for some given sources within cluster Y, some equivalent sources located at $\{\mathbf{b}_i\}$ are obtained by firstly evaluating check potentials located at $\{\mathbf{a}_i\} \in X$ and next a transformation with matrix $\boldsymbol{D}$. Then, $\sum_i G(\mathbf{a}_m,\mathbf{y}_i) q_i$ could be regarded as the check potential at the CS, which can be chosen as the boundary of X and this treatment will be discussed further later. It is noted that Eq. (17) is valid only in the given $\boldsymbol{l}$ direction, so $\sum_i G(\mathbf{a}_m,\mathbf{y}_i) q_i$ is called the upward directional check potential in $\boldsymbol{l}$ direction. Similarly, $\left(\sum_m d_{nm} \sum_i G(\mathbf{a}_m,\mathbf{y}_i) q_i\right)$ is called the upward directional equivalent source in $\boldsymbol{l}$ direction, and the boundary of X and Y are call the upward directional CS and ES in $\boldsymbol{l}$ direction respectively.

On the downward pass, by changing some indicators and recombining different items, the L2L translation can be described in Eq. (18), and the similar definition will not be repeated here.

$$\left| \sum_i G(\mathbf{x}_i,\mathbf{y}) q_i - \sum_m G(\mathbf{a}_m,\mathbf{y}) \left(\sum_n d_{nm} \sum_i G(\mathbf{x}_i,\mathbf{b}_n) q_i \right) \right| = O(\varepsilon) \tag{18}$$

Definitely, the key point of matrix decomposition Eq. (16) is how to obtain appropriate equivalent points (check points) from X (Y) and construct a suitable transformation matrix $\boldsymbol{D}$. In reference [32,36], the original method is computationally cumbersome and may not be stable enough. By using potential theory and introducing posteriori estimates, this paper proposes an improved method to construct the matrix decomposition.

Before matrix reconstruction, we first need to construct a sample matrix $\boldsymbol{G}$. The matrix $\boldsymbol{G}$ is formed by two clusters X and Y defined in Eq. (13), then it is natural to distribute dense points within the domain so that maximum characteristics could be contained in such a matrix.

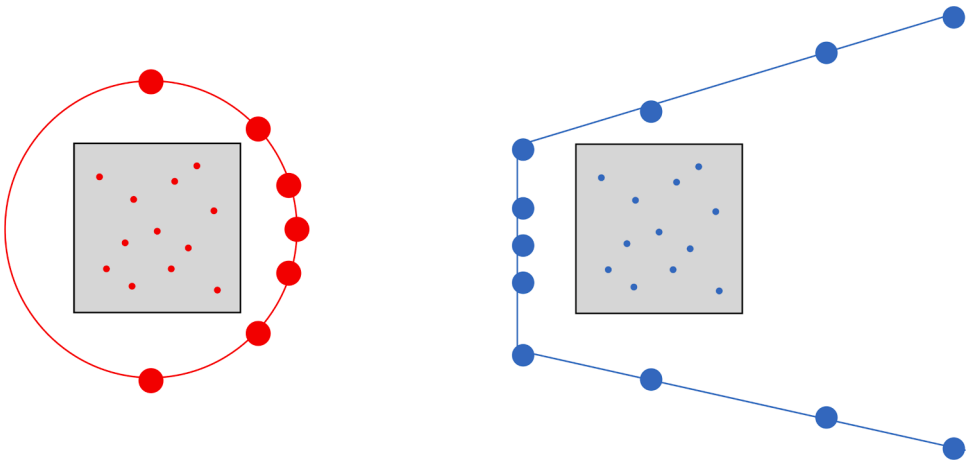

Fig. 5. Equivalent points and check points of high-frequency domain.

However, especially in 3D, the total number of points can be large for a fixed number of points per wavelength, which makes the subsequent series of matrix operations more expensive to calculate. The potential theory can be applied to simplify sampling and reduce the size of the original matrix. As mentioned in KIFMM, for sources inside an object, some equivalent sources on the surface of the object are able to evaluate the potential of the far field. In other words, the equivalent sources distributed on the boundary of the X could approximate sources inside the X. Due to the symmetry of the kernel function, it also applies to the cluster Y. And sampling points only on the boundary of X and Y, the matrix $\boldsymbol{G}$ can be obtained with all the information of these two clusters.

Furthermore, according to the numerical results studied, there are two important phenomena which would reduce sample points on X and Y. As shown in Fig. 5, the distribution of equivalent points is often concentrated in the part close to the middle region, and sparse in places far away from the middle region. In fact, this phenomenon occurs not only on the high-frequency domain, but also on the low-frequency domain. In KIFMM, the uniformly distributed equivalent points of a cell are applied to deal with interactions with the other cells from different directions. If the interaction of two cells is taken into account individually, considering a unique distribution with least points under certain accuracy, the distribution of points analogous to Fig. 5 can be found in KIFMM. Another phenomenon is that the accuracy of the matrix decomposition (equivalent approximation) is relatively insensitive to the specific position of equivalent points. Due to different ES and sample density which is used in the computation in practice, some different distributions could be obtained under the same accuracy. Although the distribution trend is the same, the equivalent points in different distributions have certain positional deviations. In this regard, a scheme for selecting sampling points with dense center and sparse ends can be adopted to further reduce the number of sample points.

Secondly, equivalent points and check points will be determined. In this section, appropriate rows and columns should be selected to span the row vector space and column vector space of the matrix $\boldsymbol{G}$. A few conventional matrix decomposition techniques have been developed quite maturely, and the pivoted QR factorization would be used to select the appropriate columns of $\boldsymbol{G}$. For the given matrix, its pivoted QR factorization can be expressed as:

$$\boldsymbol{GP} = \boldsymbol{QR} \tag{19}$$

where $\boldsymbol{P}$ is a permutation matrix which exchanges matrix column ordering, $\boldsymbol{Q}$ is a unitary matrix whose columns are orthogonal, and $\boldsymbol{R}$ is an upper triangular matrix whose diagonal elements are arranged in order of magnitude. Part of the orthogonal bases of $\boldsymbol{Q}$ can be applied to approximate the matrix $\boldsymbol{G}$. Based on the required accuracy ε, the related first few columns of $\boldsymbol{Q}$ and rows of $\boldsymbol{R}$ are denoted as $\boldsymbol{Q}_c$ and $\boldsymbol{R}_c$ respectively. Then the matrix approximation can be expressed as:

$$\left|\boldsymbol{G} - \boldsymbol{Q}_c\boldsymbol{R}_c\boldsymbol{P}^T\right| = O(\varepsilon) \tag{20}$$

where the column vector group of matrix $\boldsymbol{Q}_c$ can approximately form the column vector space of matrix $\boldsymbol{G}$. Matrix $\boldsymbol{Q}_c$ is obtained by Schmidt orthogonalization using a part of $\boldsymbol{G}$. Denote these columns of $\boldsymbol{G}$ as $\boldsymbol{G}_c$, and the corresponding sample points are the final equivalent points $\{\mathbf{b}_i\}$ on the boundary of Y.

Applying similar approach, we can obtain the representative rows $\boldsymbol{G}_r$ and the final check points $\{\mathbf{a}_i\}$ on the boundary of X.

The last step is to construct the intermediate transformation matrix $\boldsymbol{D}$. Since two bases $\boldsymbol{G}_c$, and $\boldsymbol{G}_r$ approximately span column vector space and row vector space, the following $\boldsymbol{D}$ matrix can be constructed in order to satisfy Eq. (16):

$$\boldsymbol{D} = (\boldsymbol{G}_c)^{\dagger}\boldsymbol{G}(\boldsymbol{G}_r)^{\dagger} \tag{21}$$

In Eq. (21), all matrices on the right hand side have the same numerical rank, which ensures that the matrix $\boldsymbol{D}$ of the left hand side would be full rank. By the way, the number of columns in $\boldsymbol{G}_c$, and rows in $\boldsymbol{G}_r$ is almost the same. As mentioned in Eq. (14), the numerical rank is around the number $T(\varepsilon)$.

4. Algorithm for the half space problem

Expansions of the single-layer potential G is formulated in Section 3, and a multi-level FMM is described for the half space problem in this section. The kernel function of half space problems is different from that of full space problems, which leads to some differences in the fast algorithm.

4.1. Tree structure and precomputation of translation matrices

In this paper, like other FMMs, an octree is used to divide the computational domain into different boxes, which are also called cells. A cubic box which contains the entire computational domain is established at the top level, the 0th level. In general, the bigger cell of parent level is divided into eight smaller cells of the child level by level until the number of elements in the box is smaller than a given number.

The tree structure is divided into two parts, low-frequency levels and high-frequency levels. For a cell B on level l, its interactions with other cells are different on different frequency domain and depend on the dimensionless wavenumber kw, where w is the length of cell B. And level l is defined as the high-frequency level if $kw > c_1\lambda$, otherwise it is defined as the low-frequency level. In this paper, λ is the wave length and $c_1 = \sqrt{3}$ is a corresponding coefficient. According to the distance conditions

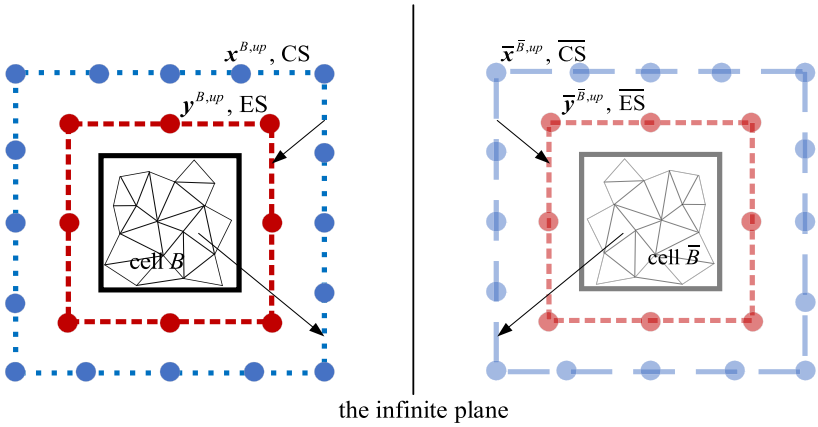

Fig. 6. The S2M translations.

required in Eq. (13), not all the levels are taken into account. The level which has no interactions between cells would be omitted, e.g. kw^2 is greater than the length of the biggest box. We denote the highest level and the bottom level of high-frequency domain as *lev_h* and *lowlev_h* respectively. No adaptive method is used to construct the octree on these high-frequency levels. And a cell of high-frequency level should be divided unless it is on *lowlev_h*. The rest levels are low-frequency levels from (*lowlev_h* + 1). We denote the bottom level of low-frequency domain as *lowlev*. Adaptive methods could be applied on low-frequency levels to decrease the computation [4].

On low-frequency levels, the near field N^B, far filed F^B, and interaction fieldI^B of a cell B are consistent with that in analytical FMM. For box B with length w, the upward ES and CS are set to be the cube center point B, and the lengths are $(1 + c_2)w$ and $(3 - c_3)w$ respectively. In this paper, c_2 and c_3 are tiny positive real numbers for which the distance between the upward ES and CS is large. Another condition $c_3 > c_2$ should also be satisfied to make sure that the equivalent sources can be approximately evaluated using the potential in F^B. In this paper, we set $c_2 = 0.05$ and $c_3 = 0.1$. Once the ES and CS are determined, translation matrices used repeatedly on upward and downward passes can be evaluated. On each low-frequency level, matrix $\boldsymbol{M}^B$ (or $\boldsymbol{S}^B$) is evaluated and stored according to Eq. (8)-(10), where $\boldsymbol{M}^B$ for M2M and $\boldsymbol{S}^B$ for S2M. No such computation of translation matrices is needed for the downward pass. As mentioned before, we have $\boldsymbol{L}^B = \left(\boldsymbol{M}^B\right)^T$ for L2L, in which the simple transposition demands nearly zero computation. It is noted that $\boldsymbol{M}$ is obtained for kernel G, not G^* of half space problems. Actually, these translation matrices can also be applied for G^* by utilizing its symmetry features, and it would be discussed later.

On high-frequency levels, the interaction field I^B is still the complementary set of cell $P(B)$'s near field, where $P(B)$ denotes the parent cell of cell B. The near field of a cell on high-frequency levels is different from that on low-frequency levels. Due to the directional parabolic separation condition, firstly the near field becomes larger and varies with the dimensionless wavenumber kw. Secondly, it is only valid in the given direction, and different expansion are obtained for each direction.

The corresponding ES and CS which satisfy the directional parabolic separation condition on high-frequency levels are set as:

$$\begin{aligned} &\text{ES}-\Gamma_Y: \quad |\boldsymbol{y}-\boldsymbol{c}_B| = \overline{w}\Big/2, \overline{w} = \sqrt{3}(1+c_2)w \\ &\text{CS}-\Gamma_X: \begin{cases} \{|\boldsymbol{x}-\boldsymbol{c}_B| = d_{ETC}, \theta(\boldsymbol{x}-\boldsymbol{c}_B, \boldsymbol{u}) \le c_4/k\overline{w}\} \cap \\ \quad \{d_{ETC} + 4k\overline{w}^2 \ge |\boldsymbol{x}-\boldsymbol{c}_B| \ge d_{ETC}, \\ d_{ETC} = \max(2.5, c_5 \cdot k\overline{w}) \cdot \overline{w} - 0.55\overline{w}\} \end{cases} \end{aligned} \tag{22}$$

where c_4 and c_5 are coefficients which determine the span angle and distance. In general, at a fixed cell size and wavenumber, the numerical rank of $\boldsymbol{G}$ increases as c_4 increases and decreases as c_5 increases under a certain accuracy. In this paper, we set $c_4 = 2.0$ and $c_5 = 0.5$. Due to improper parameter settings, the near field distance may be too small. And the near field of a cell on the high-frequency level contains at least two cells in the circumferential direction.

A uniformly distributed structured mesh on the surface of a cube is mapped to a sphere surface, and different directions are obtained from the center of an element. On the bottom level *lowlev_h* of high-frequency domain, the number of total directions is $6 \times (n_d)^2$, where $n_d = \left[\frac{\pi}{2}/\left(c_4/k\overline{w}_{lowlev\_h}\right)\right] + 1$. Its parent level (*lowlev_h* + 1) would be divided into $4 \times 6 \times (n_d)^2$ directions with the span angle decreased by a half in Eq. (22), similarly for the rest high-frequency levels.

Although there are many expansions on high-frequency levels, the transformation matrix $\boldsymbol{D}$ is computed only once on each level. For a high-frequency level, a standard configuration of CS and ES is established, and final equivalent points $\{\mathbf{a}_i\}$ and the transformation matrix $\boldsymbol{D}$ are obtained from this configuration. This matrix $\boldsymbol{D}$ can be applied to all expansions of different directions on the same level. According to coordinates rotation, the equivalent points of different directions are obtained and different expansions can be quickly constructed.

4.2. Translations of half space problems

The BIE of half space problems is almost the same as that of full space problems, expect that an additional term occurs in the kernel function of half space problems. Some researchers regard $G^*(\mathbf{x}, \mathbf{y})$ as a whole, and a large hierarchical tree which contains the structure above the infinite plane and its mirror image below the infinite plane needs to be built. With the distance between the structure and the infinite plane increasing, the computational deficiency becomes significant. For an alternative approach, $G^*(\mathbf{x}, \mathbf{y})$ could be divided into two parts and construct different expansions separately. For the first part $G(\mathbf{x}, \mathbf{y})$, its translations have been discussed in previous sections. For another part $G(\overline{\mathbf{x}}, \mathbf{y})$, only parts of translations need to be rebuilt by utilizing the symmetry of mirror images.

A tree tre_1 which contains only the above structure is constructed and we obtain all equivalent points and source intensities of each cell. And a rough tree tre_2 is also built to divide the mirror part below, yet with no specific information of ES, CS or source intensities.

Consider the S2M translation on low-frequency levels, and the first step of approximation of far field integrals. Taking only $G(\mathbf{x}, \mathbf{y})$ into consideration, cell B's equivalent points and densities are obtained by firstly evaluating the potential on the CS and then solving a Dirichlet boundary value problem inversely. For the second part $G(\overline{\mathbf{x}}, \mathbf{y})$, it would be changed slightly into $G(\mathbf{x}, \overline{\mathbf{y}})$. According to the variable symmetry of the Green's function, $G^*(\mathbf{x}, \mathbf{y}) = G(\mathbf{x}, \mathbf{y}) + G(\overline{\mathbf{x}}, \mathbf{y}) \equiv G(\mathbf{x}, \mathbf{y}) + G(\mathbf{x}, \overline{\mathbf{y}})$. As shown in Fig. 6, a set of CS and ES is established and $\overline{(\ldots)}$ denotes the

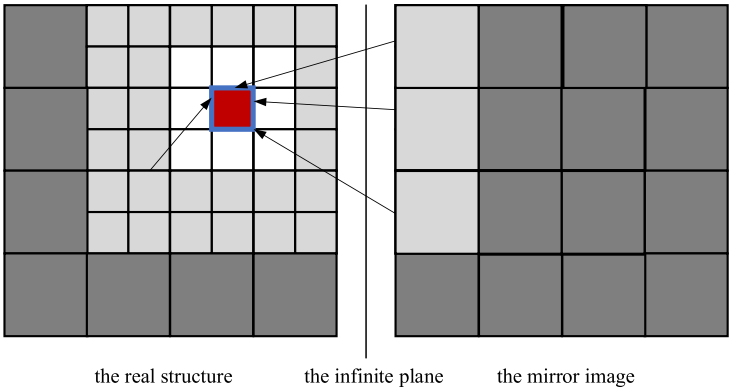

Fig. 7. The M2L translations for half space problems.

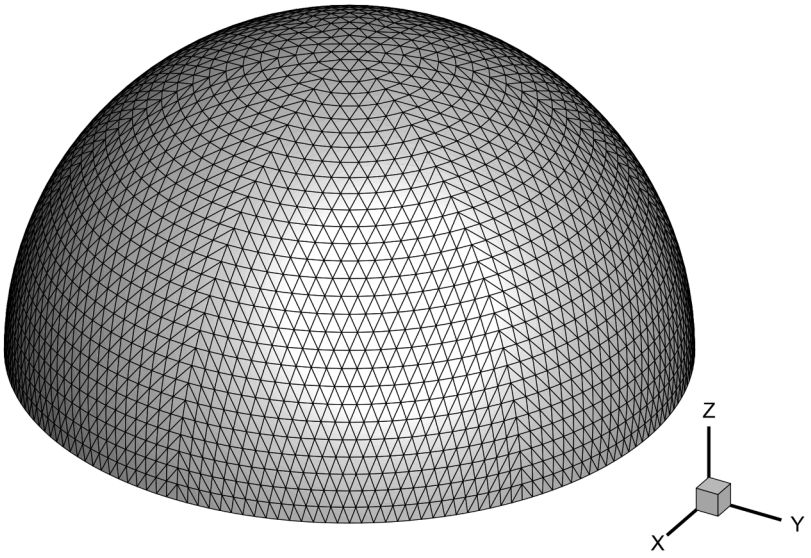

Fig. 8. A radiating hemisphere discretized with 5400 elements at $ka = 12$.

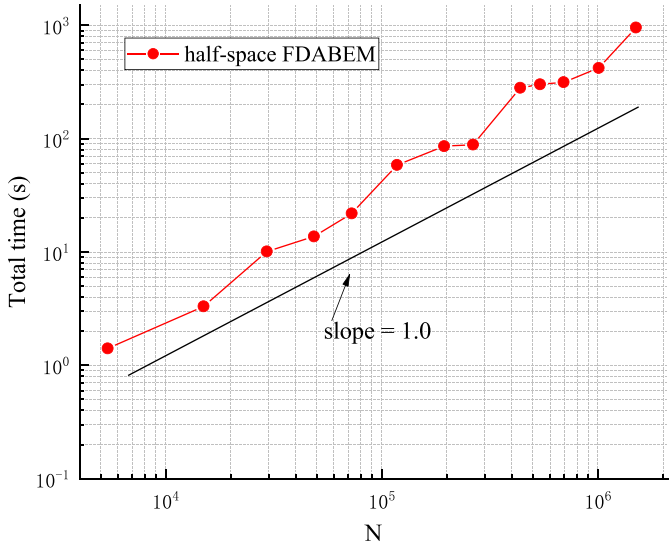

Fig. 9. The total computational time for the hemisphere radiation problem.

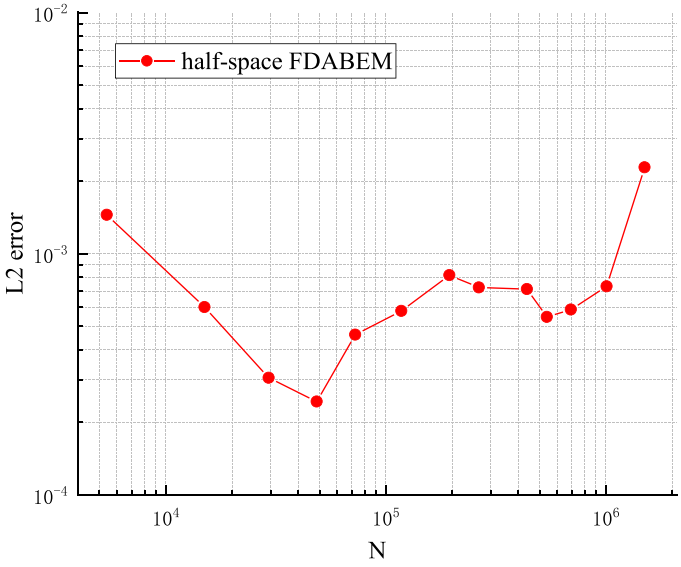

Fig. 10. The global $L2$ error on the boundary for the hemisphere radiation problem.

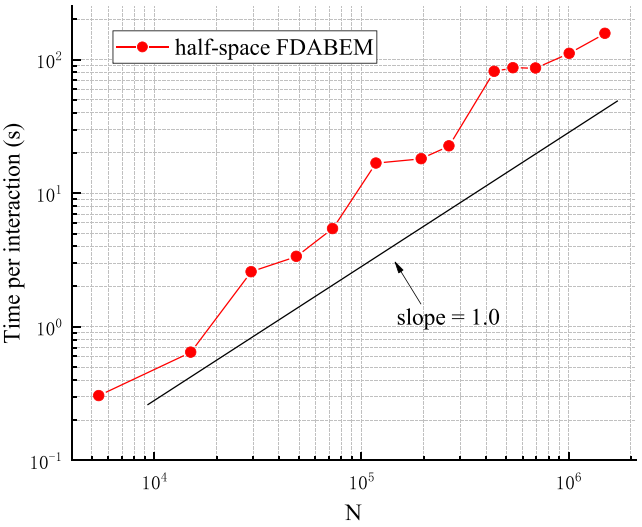

Fig. 12. The time per interaction for the hemisphere radiation problem.

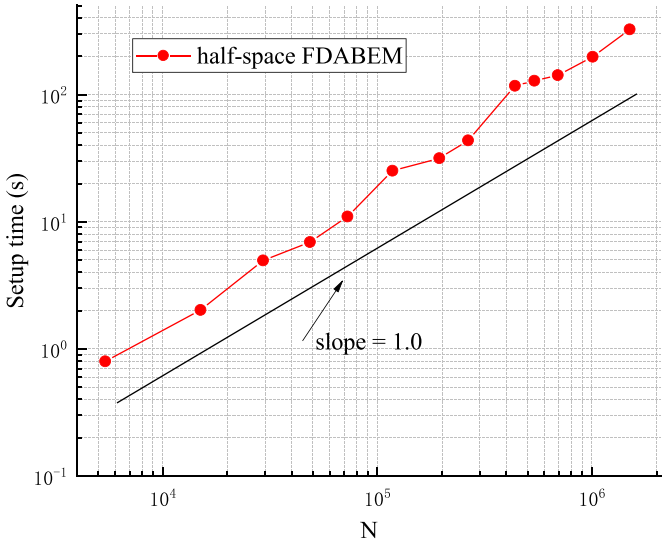

Fig. 11. The setup time for the hemisphere radiation problem.

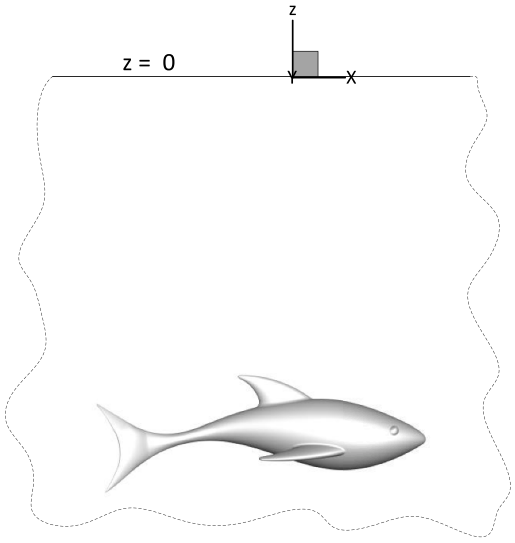

Fig. 13. The scattering problem of a fish in water.

corresponding term in tre_2. Following similar approximations in Eq. (8), the equivalent points and densities associated with $G(\mathbf{x},\overline{\mathbf{y}})$ can be obtained:

$$\phi_{\overline{n}}^{\overline{B},up}=\sum_{\overline{l}}G(\overline{\mathbf{x}}_{\overline{n}}^{\overline{B},up},\overline{\mathbf{y}}_{\overline{l}}^{\overline{B}})q_{\overline{l}}^{\overline{B}}=\sum_{\overline{m}}G(\overline{\mathbf{x}}_{\overline{n}}^{\overline{B},up},\overline{\mathbf{y}}_{\overline{m}}^{\overline{B},up})q_{\overline{m}}^{\overline{B},up} \tag{23}$$

$$\boldsymbol{E}^{\overline{B}}\boldsymbol{q}^{\overline{B}}=\boldsymbol{E}^{\overline{B},up}\boldsymbol{q}^{\overline{B},up} \tag{24}$$

$$\boldsymbol{q}^{\overline{B},up}=\left(\boldsymbol{E}^{\overline{B},up}\right)^{\dagger}\boldsymbol{E}^{\overline{B}}\boldsymbol{q}^{\overline{B}}=\boldsymbol{M}^{\overline{B}}\boldsymbol{q}^{\overline{B}} \tag{25}$$

Comparing Eqs. (8)-(10) and Eqs. (23)-(25) in the expressions, the only difference is the index. Naturally, if the configuration of ES, CS and equivalent points is built as same as that in tre_1, then matrices appeared in Eq. (25) would be consistent with that in Eq. (10). No more additional computation is needed on the S2M translation associated with function $G(\mathbf{x},\overline{\mathbf{y}})$.

Similar conclusions apply to the M2M translation. On the upward pass, the equivalent points and densities of mirror cells in tre_2 are easily obtained by the utilizing the symmetry with a specific configuration of ES and CS.

As mentioned before, the L2L translation can be regarded as an inverse of the M2M translation. Once the location and densities of equivalent points are determined, the potential of each cell above the infinite plane can be obtained, and the L2L translation only occurs in tre_1.

In half space problems, the M2L translation is slightly different from that in full space problems. In full space problems, the interaction filed I^B of cell B is around the cell itself. In half space problems, the contribution of mirror cells also needs to be taken into account. Some simplification measures are taken to further decrease the M2L computation of mirror cells. An example on level 3 is shown in Fig. 7. For a cell B (marked in red) on level 3, there are four types of cells which contribute to its potential on the downward CS (marked in blue). On the real part, light grey cells in I^B perform direct M2L translations to B; dark grey cells have performed direct M2L translations to $P(B)$, and the check potential of $P(B)$ is transferred to B through a standard L2L translation. On the mirror part, there are two similar types of cells, and the

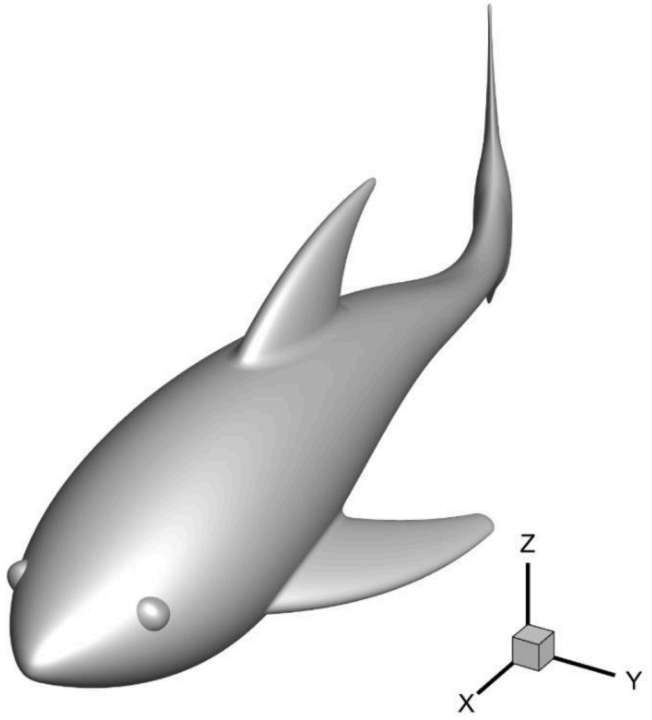

Fig. 14. Geometry of the fish.

difference is that cells on the parent level is also contained in I^B. Introducing cells from other levels into the M2L translation of the current level cell will further decrease the total time of M2L operation, which is the most time-consuming step. In fact, this effect is more significant when the structure is far away from the infinite plane. When the distance between the structure and the infinite plane is large enough, for example larger than the size of the structure itself, only additional M2L translations on level 2 are needed for the mirror part.

Similarly, on high-frequency levels of half space problems, only the M2L operation of five translations needs an additional contribution of mirror cells. Different from the fast algorithm on low-frequency levels, the equivalent source of the mirror cell and the check potential of the real cell are directional and the determination of the interaction field is more complicated. The other translations are the same as those in full space problems, and no additional calculations are introduced.

5. Numerical examples

Numerical examples are presented in this section to demonstrate the accuracy and efficiency of the developed wideband half-space FDABEM for 3-D half-space acoustic problems. The computer code is implemented in Fortran. All numerical examples are performed on a workstation, for which the CPU is an Intel Xeon Gold 6448Y at 2.10 GHz. The acceleration with OpenMP is used in parts of the code and 16 threads are applied. The tolerance for convergence of the iterative solver GMRES is set to 1E-3.

In this paper, the infinite plane is set as $z = 0$. For the cell B with length d on level l, the level l is regarded as a high-frequency level if $kd \geq \sqrt{3}\pi$, otherwise it is regarded as a low-frequency level. On low-frequency levels, squares are utilized to establish ES and CS and 98 equivalent points are evenly distributed on the upward ES. On high-frequency levels, spheres and conical cylinders are utilized to establish the upward directional ES and CS, and the number of equivalent points is determined by the required accuracy (1E-4). These settings on the low and high frequency levels ensures that the accuracy of the fast algorithm is above the GMRES tolerance.

5.1. A hemisphere radiation problem

First, a benchmark case is studied to demonstrate the accuracy and efficiency of the algorithm. Considering a unit hemisphere on the infinite plane $z = 0$, all particles on the surface of the hemisphere pulsate with the same normal velocity and the symmetry infinite plane is set as a sound hard surface. Given $q = 1$, the pressure on the hemisphere can be expressed as an analytical solution: $\phi = 1/(1 - ik)$. The global $L2$ error on the boundary is defined as:

$$L2\text{Error} = \sqrt{\frac{\sum_i \left|\phi_i^{\text{ana}} - \phi_i^{\text{FDA}}\right|^2}{\sum_i \left|\phi_i^{\text{ana}}\right|^2}} \tag{26}$$

in which ϕ^{ana} is the analytical solution on the boundary and ϕ^{FDA} is the numerical solution by using the half-space FDABEM.

For this radiation problem, the hemisphere surface is discretized by

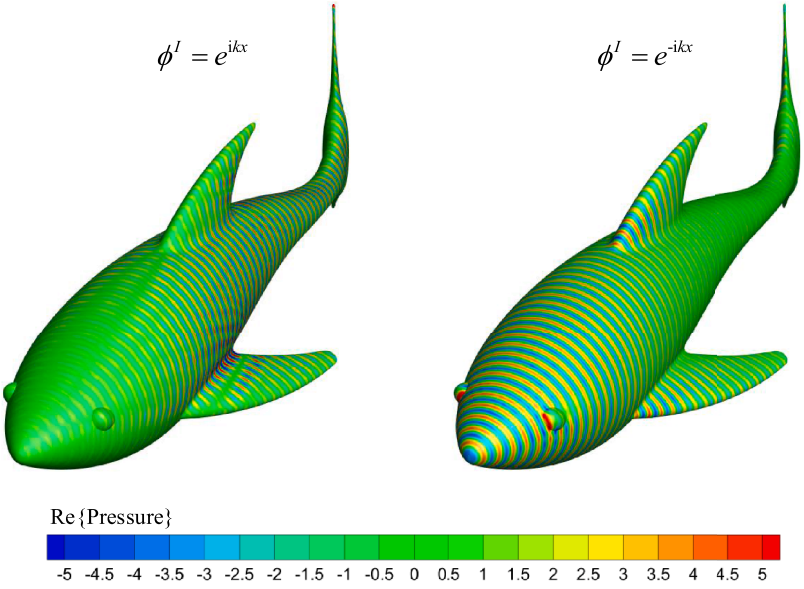

Fig. 15. Contour plot of the sound pressure of the underwater fish.

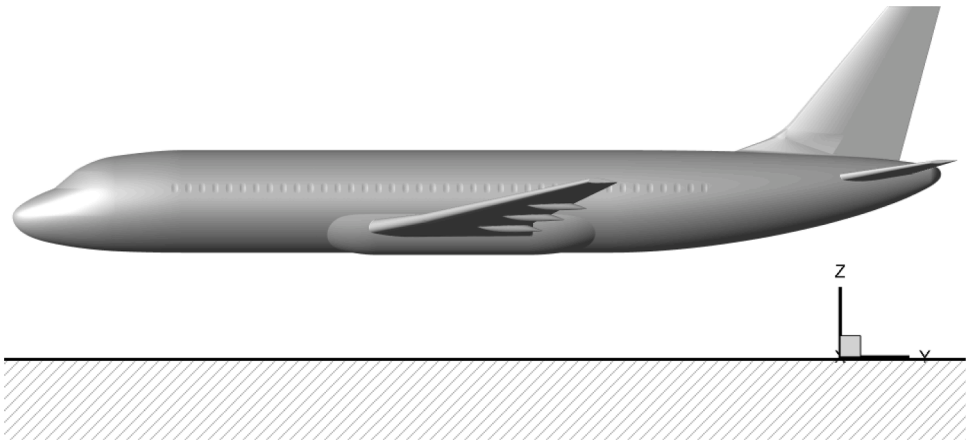

Fig. 16. Geometry of the airplane model.

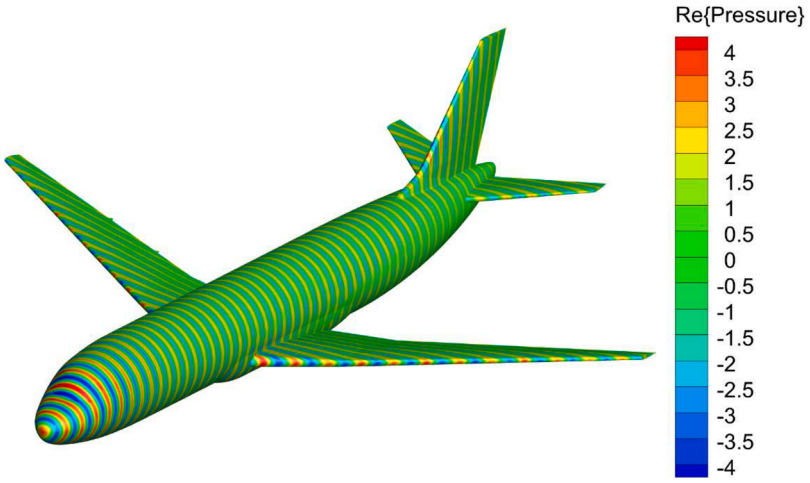

Fig. 17. Contour plot of the pressure of the airplane scattering problem.

piecewise triangular constant elements with 20 elements per wavelength. The dimensionless wavenumber ka of this example ranges from 12 to 300, and the degree of freedom N ranges from 5400 to 1500,000. For The smallest model with $ka = 12$ shown in Fig. 8, the number of elements in this case is slightly increased to reduce the error in representing the geometry.

The total computation time consists of setup time and iterative solution time with GMRES. In the setup step, the matrices that are utilized repeatedly in the loop iteration calculation will be stored. For example, various translation matrices on each level of the tree structure are calculated once and stored. The contributions of the near-field integrals are first grouped into a matrix and only matrix-vector products are performed in each subsequent iteration, thus avoiding repeated calculations of the near-field integrals. Figs. 9–12 show the total computation time, the global $L2$ error on the boundary, the setup time and the time per interaction, respectively. It is shown that numerical results agree very well with the analytical solution. All the computation times of the three indicators increase approximately linearly with the number of DOFs.

In addition, a special numerical example is designed to demonstrate the effectiveness of the Burton-Miller formulation. The wavenumber is set as 62.83 m^{-1}, so the dimensionless wavenumber ka is 125.66 ($\approx 40\pi$), which is a fictitious eigenfrequency for the exterior problem with the Neumann boundary condition. The numerical solution also agrees very well with the analytical solution and the global $L2$ error over the boundary is 1.44E-3.

5.2. Fish scattering problem

This example considers the scattering problem of a fish underwater as shown in Fig. 13. The characteristic length of the fish along the body is about 0.3 >m and the centroid of the fish is about 0.5 m from the horizontal infinite plane. The geometry is shown in Fig. 14. In this example, the dimensionless wavenumber ka is set as 440, about 70 wavelengths. The incident plane wave is defined as $\phi^I = e^{ik\boldsymbol{x}\cdot\boldsymbol{d}}$ with the wave propagating direction $\boldsymbol{d}_1 = (1, 0, 0)$ and $\boldsymbol{d}_2 = (-1, 0, 0)$. The boundary of the fish is discretized with 3435,794 piecewise triangular constant elements. The real part of the computed sound pressure is shown in Fig. 15.

For $\boldsymbol{d}_1 = (1, 0, 0)$, the total computation time is 26,478 s, in which the setup time is 546 s and the iterative solution time is 25,932 s. It takes 122 iterations to solve this problem, and the computation time for each iteration is about 217 s.

For $\boldsymbol{d}_2 = (-1, 0, 0)$, the total computation time is 28,992 s, in which the setup time is 551 s and the iterative solution time is 28,441 s. It takes 133 iterations to solve this problem, and the computation time for each iteration is about 212 s.

5.3. An airplane scattering problem

For the third example, we considered a scattering problem with the incident wave impinging on the front of an airplane model. The infinite plane and surfaces of the airplane are set to be sound hard. As shown in

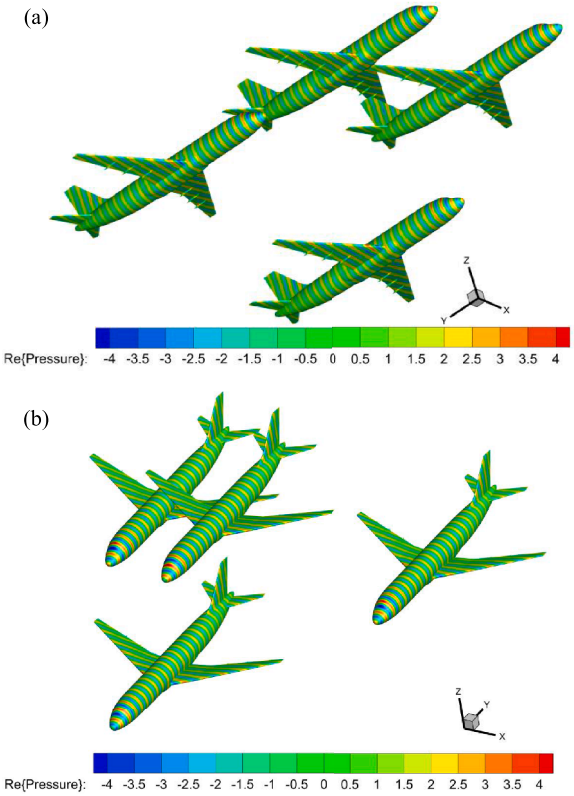

Fig. 18. Contour plots of the pressure of the multi-airplane scattering problem: (a) View of looking up; (b) View of looking down.

Fig. 16, the length in *x, y, z* directions of the airplane are about 100 m, 130 m and 33 m, respectively. The bottom of the airplane is about 13 m from the infinite plane (ground). The dimensionless wavenumber considered in this example is $ka = 340$, which is about 54 wavelengths. The incident plane wave is defined as $\phi^{\mathrm{I}} = e^{ik\boldsymbol{x}\cdot\boldsymbol{d}}$, with the wave propagating direction $\boldsymbol{d} = (0, 1, 0)$. The surface of the airplane is discretized into 2955,457 piecewise triangular constant elements. The total computation time is 15,975 s, in which the setup time is 507 s and the iterative computation time is 15,468 s. It takes 72 iterations to solve this model, and the computation time for each iteration is about 212 s. The contour plot of the sound pressure is shown in Fig. 17.

Finally, we consider a multiple aircraft model, the bottom of which is also 13 m from the ground, and a total of 3391,840 constant elements are used to discretize the boundary. The direction of the incident plane wave is consistent with the single-plane model above. The dimensionless wavenumber *ka* considered in this example is also 340. The total computation time is 86,862 s, in which the setup time is 488 s and the iterative computation time is 86,374 s. It takes 473 iterations to solve this model, and the computation time for each iteration is about 182 s. The contour plot of the sound pressure is shown in Fig. 18.

6. Conclusion

In this paper, a kernel-independent fast multipole BEM based on the fast directional algorithm is proposed to solve 3-D half-space acoustic wave problems. On high-frequency levels in the tree structure, only sampling sparse points on the directional check or equivalent surface are used to construct the sample matrix which contains enough information for the interaction between the two clusters. The Green's function for half-space problems is divided into two symmetrical parts, and similar translations as for the full-space FMM are employed. By utilizing the symmetry, only the M2L translations of the image part are added to the total computation. In addition, the number of M2L translations of the image part can be smaller than that of the original part. The OpenMP programming is used to further improve the computational efficiency of the proposed half-space FDABEM. Numerical examples solved on a workstation, including those with the number of DOFs above 3 million and *ka* above 400, clearly demonstrate the high accuracy and $O(N\log N)$ computation complexity of the developed FDABEM.

Due to the kernel-independent properties of the present method, the developed method can be adapted to solve other half-space problems readily, besides for the Helmholtz equation. Only parts of the code are parallelized in this work. Full parallelization and the GPU acceleration can be considered in the future to further improve the computational efficiency of the developed method and code.

CRediT authorship contribution statement

Haoyang Li: Writing – original draft, Visualization, Validation, Software, Investigation, Formal analysis, Data curation. **Yijun Liu:** Writing – review & editing, Supervision, Resources, Project administration, Methodology, Investigation, Funding acquisition, Conceptualization.

Declaration of competing interest

The authors declare the following financial interests/personal relationships which may be considered as potential competing interests: Yijun Liu reports financial support was provided by National Natural Science Foundation of China. If there are other authors, they declare that they have no known competing financial interests or personal relationships that could have appeared to influence the work reported in this paper.

Acknowledgments

The authors would like to thank the financial support from the National Natural Science Foundation of China (Project Nos. 11972179 and 12372198).

Data availability

Data will be made available on request.

References

[1] Seybert AF, Soenarko B, Rizzo FJ, Shippy DJ. An advanced computational method for radiation and scattering of acoustic-waves in 3 dimensions. J Acoust Soc Am 1985;77(2):362–8.
[2] Liu YJ, Rizzo FJ. A weakly singular form of the hypersingular boundary integral-equation applied to 3-D acoustic-wave problems. Comput Methods Appl Mech Eng 1992;96(2):271–87.
[3] Bai MR. Application of BEM (boundary element method)-based acoustic holography to radiation analysis of sound sources with arbitrarily shaped geometries. J Acoust Soc Am 1992;92(1):533–49.
[4] Shen L, Liu YJ. An adaptive fast multipole boundary element method for three-dimensional acoustic wave problems based on the Burton-Miller formulation. Comput Mech 2007;40(3):461–72.
[5] Liu YJ, Mukherjee S, Nishimura N, Schanz M, Ye W, Sutradhar A, Pan E, Dumont NA, Frangi A, Saez A. Recent advances and emerging applications of the boundary element method. Appl Mech Rev 2011;64(3).
[6] Peake MJ, Trevelyan J, Coates G. Extended isogeometric boundary element method (XIBEM) for two-dimensional Helmholtz problems. Comput Methods Appl Mech Eng 2013;259:93–102.
[7] Kirkup S. The boundary element method in acoustics: a survey. Appl Sci-Basel 2019;9(8).
[8] Liu YJ. On the BEM for acoustic wave problems. Eng Anal Bound Elem 2019;107:53–62.
[9] Venås JV, Kvamsdal T. Isogeometric boundary element method for acoustic scattering by a submarine. Comput Methods Appl Mech Eng 2020;359.
[10] Liu YJ. Fast multipole boundary element method - Theory and applications in engineering. Cambridge: Cambridge University Press; 2009.
[11] Pan EN, Chen CS, Amadei B. A BEM formulation for anisotropic half-plane problems. Eng Anal Bound Elem 1997;20(3):185–95.

[12] Seybert AF, Soenarko B. Radiation and scattering of acoustic-waves from bodies of arbitrary shape in a 3-dimensional half-space. J Vibrat Acoustics Stress Reliabil Design-Trans Asme 1988;110(1):112–7.
[13] Triantafyllidis T. 3-D time domain bem using half-space green-functions. Eng Anal Bound Elem 1991;8(3):115–24.
[14] Bapat MS, Shen L, Liu YJ. Adaptive fast multipole boundary element method for three-dimensional half-space acoustic wave problems. Eng Anal Bound Elem 2009;33(8–9):1113–23.
[15] Wu H, Liu Y, Jiang W, Lu W. A fast multipole boundary element method for three-dimensional half-space acoustic wave problems over an impedance plane. Int J Comput Methods 2015;12(01).
[16] Greengard L, Rokhlin V. A fast algorithm for particle simulations. J Comput Phys 1987;73(2):325–48.
[17] Yasuda Y, Oshima T, Sakuma T, Gunawan A, Masumoto T. Fast multipole boundary element method for low-frequency acoustic problems based on a variety of formulations. J Comput Acoust 2010;18(4):363–95.
[18] Yasuda Y, Higuchi K, Oshima T, Sakuma T. Efficient technique in low-frequency fast multipole boundary element method for plane-symmetric acoustic problems. Eng Anal Bound Elem 2012;36(10):1493–501.
[19] Wang XH, Zhang XM, Zhang JM, Zheng XS. An adaptive expansion technique in the fast multipole method for 3D acoustics problems at low frequencies. Eng Anal Bound Elem 2014;46:93–5.
[20] Rahola J. Diagonal forms of the translation operators in the fast multipole algorithm for scattering problems. BIT 1996;36(2):333–58.
[21] Cheng H, Greengard L, Rokhlin V. A fast adaptive multipole algorithm in three dimensions. J Comput Phys 1999;155(2):468–98.
[22] Wu HJ, Liu YJ, Jiang WK. Analytical integration of the moments in the diagonal form fast multipole boundary element method for 3-D acoustic wave problems. Eng Anal Bound Elem 2012;36(2):248–54.
[23] Cheng HW, Crutchfield WY, Gimbutas Z, Greengard LF, Ethridge JF, Huang JF, Rokhlin V, Yarvin N, Zhao JS. A wideband fast multipole method for the Helmholtz equation in three dimensions. J Comput Phys 2006;216(1):300–25.
[24] Wolf WR, Lele SK. Wideband fast multipole boundary element method: application to acoustic scattering from aerodynamic bodies. Int J Numer Methods Fluids 2010;67(12):2108–29.
[25] Zheng CJ, Matsumoto T, Takahashi T, Chen HB. A wideband fast multipole boundary element method for three dimensional acoustic shape sensitivity analysis based on direct differentiation method. Eng Anal Bound Elem 2012;36(3):361–71.
[26] Li J, Chen W, Qin Q. A modified dual-level fast multipole boundary element method based on the Burton–Miller formulation for large-scale three-dimensional sound field analysis. Comput Methods Appl Mech Eng 2018;340:121–46.
[27] Li Y, Atak O, Desmet W. Novel and efficient implementation of multi-level fast multipole indirect BEM for industrial Helmholtz problems. Eng Anal Bound Elem 2024;159:150–63.
[28] Ying L, Biros G, Zorin D. A kernel-independent adaptive fast multipole algorithm in two and three dimensions. J Comput Phys 2004;196(2):591–626.
[29] Rejwer-Kosińska E, Rybarska-Rusinek L, Linkov A. On evaluation of local fields by fast multipole method employing smooth equivalent/check surfaces. Appl Math Comput 2021;408.
[30] Rejwer-Kosińska E, Rybarska-Rusinek L, Linkov A. On accuracy of translations by kernel independent fast multipole methods. Comput Math Appl 2022;124:227–40.
[31] Engquist B, Ying L. Fast directional multilevel algorithms for oscillatory kernels. SIAM J Sci Comput 2007;29(4):1710–37.
[32] Messner M, Schanz M, Darve E. Fast directional multilevel summation for oscillatory kernels based on Chebyshev interpolation. J Comput Phys 2012;231(4):1175–96.
[33] Benson AR, Poulson J, Tran K, Engquist B, Ying LX. A parallel directional fast multipole method. SIAM J Sci Comput 2014;36(4):C335–52.
[34] Börm S. Adaptive directional compression of high-frequency Helmholtz boundary element matrices. Comput Meth Appl Mat 2021;21(3):513–27.
[35] Cao Y, Wen L, Xiao J, Liu Y. A fast directional BEM for large-scale acoustic problems based on the Burton–Miller formulation. Eng Anal Bound Elem 2015;50:47–58.
[36] Engquist B, Ying L. Fast directional algorithms for the Helmholtz kernel. J Comput Appl Math 2010;234(6):1851–9.
[37] Cao Y, Liu J, Chen D. An explicitly-sparse representation for oscillatory kernels with wave atom-like functions. J Comput Phys 2024;497.
[38] Xing X, Chow E. Interpolative decomposition via proxy points for kernel matrices. SIAM J Matrix Anal Appl 2020;41(1):221–43.
[39] Huang H, Xing X, Chow E. H2Pack: high-performance matrix package for kernel matrices using the proxy point method. Acm Trans Math Software 2021;47(1).
[40] Wu BW, Cho MH. Robust fast direct integral equation solver for three-dimensional doubly periodic scattering problems with a large number of layers. J Comput Phys 2023;495.
[41] Minden V, Ho KL, Damle A, Ying LX. A recursive skeletonization factorization based on strong admissibility. Multiscale Model Simul 2017;15(2):768–96.
[42] Ho KL, Greengard L. A fast direct solver for structured linear systems by recursive skeletonization. SIAM J Sci Comput 2012;34(5):A2507–32.
[43] Ho KL, Ying LX. Hierarchical interpolative factorization for elliptic operators: integral equations. Commun Pure Appl Math 2016;69(7):1314–53.
[44] Corona E, Martinsson PG, Zorin D. An $O(N)$ direct solver for integral equations on the plane. Appl Comput Harmon Anal 2015;38(2):284–317.
[45] Martinsson PG, Tropp JA. Randomized numerical linear algebra: foundations and algorithms. Acta Numer 2020;29:403–572.
[46] Gopal A, Martinsson PG. An accelerated, high-order accurate direct solver for the Lippmann-Schwinger equation for acoustic scattering in the plane. Adv Comput Math 2022;48(4).
[47] Burton AJ, Miller GF. Application of integral equation methods to numerical solution of some exterior boundary-value problems. Proceed Royal Society London Series a-Math Phys Sci 1971;323(1553):201–10.